Superconducting Microstrip Losses at Microwave and Submillimeter Wavelengths

Hähnle, S.; Kouwenhoven, K.; Buijtendorp, B.; Endo, A.; Karatsu, K.; Thoen, D.; Murugesan, V.; Baselmans, J.J.A.

Important note
To cite this publication, please use the final published version (if applicable).
Please check the document version above.

Editors' Suggestion

Superconducting Microstrip Losses at Microwave and Submillimeter Wavelengths

S. Hähnle[1,2,*] K. Kouwenhoven[1,2] B. Buijtendorp,[2] A. Endo[2,3] K. Karatsu,[1,2] D.J. Thoen[2]
V. Murugesan,[1] and J.J.A. Baselmans[1,2]

[1]*SRON - Netherlands Institute for Space Research, Sorbonnelaan 2, Utrecht 3584 CA, The Netherlands*

[2]*Department of Microelectronics, Faculty of Electrical Engineering, Mathematics and Computer Science (EEMCS), Delft University of Technology, Mekelweg 4, Delft 2628 CD, The Netherlands*

[3]*Kavli Institute of NanoScience, Faculty of Applied Sciences, Delft University of Technology, Lorentzweg 1, Delft 2628 CJ, The Netherlands*

We present a lab-on-chip experiment to accurately measure losses of superconducting microstrip lines at microwave and submillimeter wavelengths. The microstrips are fabricated from Nb-Ti-N, which is deposited using reactive magnetron sputtering, and amorphous silicon which is deposited using plasma-enhanced chemical vapor deposition (PECVD). Submillimeter wave losses are measured using on-chip Fabry-Perot resonators (FPRs) operating around 350 GHz. Microwave losses are measured using shunted half-wave resonators with an identical geometry and fabricated on the same chip. We measure a loss tangent of the amorphous silicon at single-photon energies of $\tan\delta = 3.7 \pm 0.5 \times 10^{-5}$ at approximately 6 GHz and $\tan\delta = 2.1 \pm 0.1 \times 10^{-4}$ at 350 GHz. These results represent very low losses for deposited dielectrics, but the submillimeter wave losses are significantly higher than the microwave losses, which cannot be understood using the standard two-level system loss model.

I. INTRODUCTION

Low-loss transmission lines are a fundamental requirement for integrated superconducting devices operating at both microwave and submillimeter wavelengths. At microwave frequencies, the primary driver for low-loss transmission lines is the development of qubits [1,2] and microwave kinetic inductance detectors (MKIDs) [3,4] based on high-quality factor resonators[5,6], as well as parametric amplifiers based on very long transmission lines (Ref. [7]). In addition, high-impedance transmission lines can be used to further integrate microwave electronics onto the device chip [8,9]. All these devices are predominantly realized using coplanar waveguide (CPW) technology, achieving losses corresponding to $Q_i > 10^6$ (Ref. [5,6]). However, the planar nature of CPWs leads to large and complicated designs which can be difficult to scale. Multilayer structures such as microstrips [10] and parallel-plate capacitors [11] are preferable in order to create smaller devices and easily obtain high-impedance transmission lines, but these structures suffer from increased losses in the additional dielectric layer.

At submillimeter wave frequencies, astronomical applications rely increasingly on integrated devices, such as multicolor/multipolarization pixels [12], phased array antennas [13], and on-chip filterbanks [14–16]. These usually use microstrips, as common mode excitation and radiation loss become serious issues at higher frequencies [17,18]. However, these devices are usually based on Nb/SiO$_2$ technology, which has a 690 GHz cutoff due to the critical temperature of Nb and relatively high losses due to the SiO$_2$.

The losses of microstrips at these frequencies and sub-Kelvin temperatures are generally attributed to the existence and excitation of two-level tunneling systems (TLSs) in the bulk of the amorphous dielectric. While the macroscopic behavior of TLSs is relatively well understood, their microscopic origin is still for the most part unclear. Owing to the lack of a microscopic understanding, development and investigation of low-loss dielectrics relies heavily on iterative cycles of deposition and measurement. These loss measurements are usually only carried out at microwave frequencies, under the assumption that material properties are comparable at submillimeter frequencies based on TLS theory [19]. As a result, limited data is available at $f > 100$ GHz and $T < 1$ K, where both signal generation and detection become increasingly challenging.

Measurements comparing microwave and submillimeter wave loss were performed by Chang *et al.* [20]

and Gao *et al.* [21] on Nb/SiO$_2$/Nb microstrips at 220 and 110 GHz, respectively, and by Endo *et al.* [22] on Nb-Ti-N/SiN/Nb-Ti-N microstrips at 650 GHz. These experiments combined quasi-optical techniques with different on-chip test devices exploiting either path length differences [20] or resonant structures [21,22]. However, these approaches suffer from large intrinsic uncertainties and are not sufficiently precise to study materials with a lower loss tangent. In the case of resonant structures, this can be mitigated by using long resonators at higher mode numbers, where coupler effects are suppressed.

In this paper, we present loss measurements of superconducting Nb-Ti-N/a-Si/Nb-Ti-N microstrips at microwave and submillimeter wavelengths and at sub-Kelvin temperatures. We show TLS-like behavior at microwaves, but find a significant increase in loss at submillimeter wavelengths which is inconsistent with the TLS standard model.

II. DEVICE DESIGN

We have designed a chip which combines shunted microwave resonators (μWR) and in-line submillimeter wave Fabry-Perot resonators (FPRs). The μWR are coupled to a CPW transmission line (henceforth called readout line) which runs over the entire chip, terminating in bond pads connecting the chip to a sample holder via Al bond wires. The loss as a function of photon number can be obtained by measuring the readout line transmission around the resonance frequency of the shunted resonator and retrieving the loaded quality factor Q_L and minimum transmission $S_{21,\min}$ of the Lorentzian dip. The internal loss factor Q_i and coupling strength Q_c then follow from the dip

depth $S_{21,\min} = Q_L/Q_i$ and the loaded quality factor, which can be expressed as

$$Q_L(n) = \frac{nQ_{c,1}Q_i}{nQ_{c,1} + Q_i}, \tag{1}$$

where n is the mode number of the resonance peak and $Q_{c,1}$ is the coupling strength at $n = 1$, with $Q_c = nQ_{c,1}$ (see the Appendix).

For the submillimeter wave case, we excite the FPRs using a quasi-optical scheme, coupling radiation from a coherent source via an antenna and CPW line to the on-chip FPR. The relative power transmitted is measured as a function of source frequency using a MKID coupled to the far end of the FPR and read out using the same readout line as the μWRs. This approach was previously used to measure CPW FPRs [17].

The design of the chip is given in Fig. 1(a). Six μWRs with resonance frequencies around 6 GHz are coupled to the readout line. Of these, four are half-wave microstrip resonators using Nb-Ti-N/a-Si/Nb-Ti-N microstrips with a dielectric thickness of $h = 250$ nm and line width $w = 2$ μm, and two are quarter-wave CPW resonators with a linewidth of 6 μm and slot width of 16 μm. The CPW resonators are deposited directly on the Si substrate, with μWR6 fully implemented in the lower Nb-Ti-N layer, whereas the center line of μWR5 is implemented using the upper Nb-Ti-N layer.

We implement four FPRs on the chip, where each FPR is connected to its own separate feeding network via two identical couplers, using the design shown in Fig. 1(b).
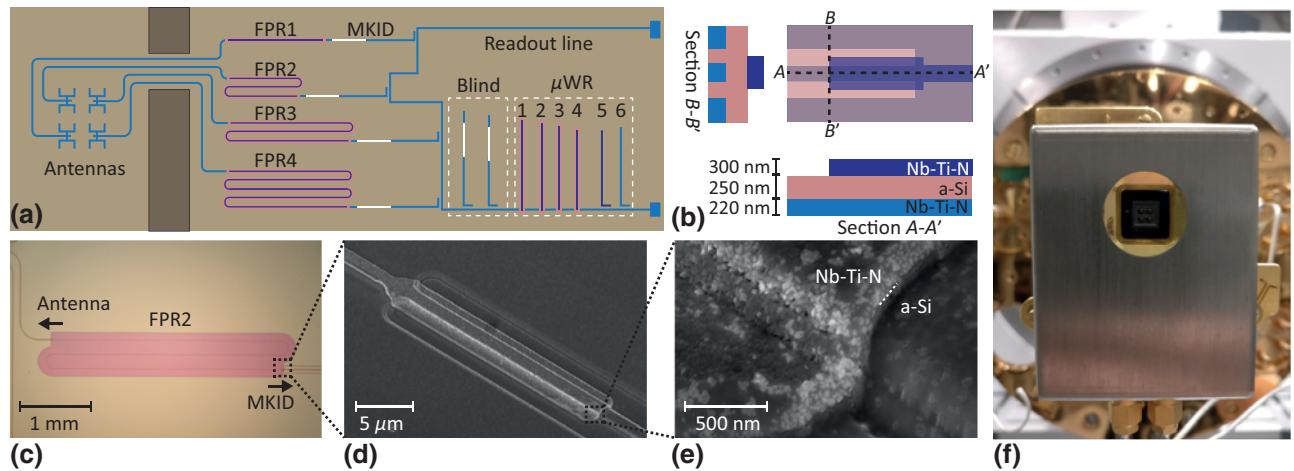
FIG. 1. (a) Chip schematic. Nb-Ti-N CPW structures are given in light blue, the Al/Nb-Ti-N CPW of the hybrid MKIDs is given in white, a-SI is shown in red, and the Nb-Ti-N microstrip lines are shown in dark blue. One of the CPW microwave resonators (μWR5) is also shown in dark blue to highlight the use of the upper Nb-Ti-N layer for the CPW center line. (b) FPR coupler schematic with two cross sections *A-A'* and *B-B'*. The schematic is shown top down with semitransparent layers, in order to clearly show the layout of the bottom Nb-Ti-N layer which is fully covered by a-Si. (c) Optical microscope image of FP2. (d) Angled scanning electron microscopy (SEM) image of the FPR coupler. (e) High-resolution SEM image of the microstrip open end. Overetch into the a-Si layer is visible, with the dotted white line indicating the border between Nb-Ti-N and a-Si. (f) Picture of the device mounted in the cryostat.

All four resonators are made with identical line and coupler geometry, but have different lengths l_{FP} (FPR1, 5 mm; FPR2, 10 mm; FPR3, 20 mm; FPR4, 50 mm). This design is chosen to obtain resonators which, for the same frequency, have different mode numbers but identical Q_i and $Q_{c,1}$.

We use a CPW with 2 μm line and gap width between the antenna and the FPR, because we know its loss to be negligible at submillimeter wave frequencies [17]. The MKIDs are quarter-wave resonators of a standard Al/Nb-Ti-N hybrid CPW design [4], where incoming power is absorbed in a short Al central line, leading to changes in the MKIDs microwave properties which are measured via the microwave readout line.

III. DEVICE FABRICATION

We start the fabrication process with a 375-μm-thick 4-in. Si wafer (dielectric constant $\epsilon_r = 11.44$; Ref. [23]) coated on both sides with a 1-μm-thick, low-tensile-stress ($\sim$ 250 MPa) SiN layer ($\epsilon_r = 7$), deposited using low-pressure chemical vapor deposition (LPCVD). The SiN on the device side is etched away almost everywhere, except for small patches below the MKID Al center lines [24]. For the FPR and μWR fabrication, we now start by depositing a 220-nm-thick Nb-Ti-N layer ($T_c = 15.1$ K, $\rho_n = 138$ $\mu\Omega$cm) on the device side using reactive sputtering of a NbTi target in a nitrogen-argon atmosphere [25]. This layer is patterned and etched to contain the microstrip ground plane and all CPW elements of the chip. A 250-nm-thick a-Si layer $\epsilon_r \approx 10$, deposited using plasma-enhanced chemical vapor deposition (PECVD), serves as the dielectric layer of the microstrip [26]. We then define the microstrip lines in a second Nb-Ti-N layer of 300 nm ($T_c = 15.0$ K, $\rho_n = 104$ $\mu\Omega$cm), using the same process as the first Nb-Ti-N layer. With the FPR and μWR finalized, we finish fabrication of the MKIDs and microwave readout line using a 1-μm-thick layer of polyimide LTC9505 and a 50-nm-thick layer of Al ($T_c = 1.25$ K) [27]. Finally, a 40-nm-thick layer of β-phase Ta ($T_c = 0.7$ K) is deposited on the backside and patterned into an absorbing mesh for stray light control [28].

As Nb-Ti-N and a-Si require the same dry etch agents, an overetch of approximately 40 nm is present for the lower layers, as highlighted in Fig. 1(e). The thickness of the lower Nb-Ti-N layer is increased accordingly to maintain designed antenna and MKID properties.

IV. EXPERIMENTAL SETUP

The μWRs are characterized in a dark cryogenic setup, which is optimized for low-background MKID experiments as discussed in [4,29], and using a standard homodyne technique enabled by a commercial vector network analyzer (VNA). In order to achieve acceptable noise levels at the low microwave powers required to reach

the single-photon regime, a -36-dB attenuation on the input, and an amplifier with 36-dB gain on the output are added to the microwave readout chain at room temperature.

For measurements of the FPR transmission, a 2×2 lens array is mounted on the chip backside and aligned to the double-slot antennas. Each lens has a hyper-hemispherical shape with 2 mm diameter, creating a diffraction-limited beam [30]. The chip is then placed in a Cu sample holder, which is surrounded by a tight-fitting mu-metal magnetic shield [see Fig. 1(f)]. This assembly is mounted on the cold stage of a dilution refrigerator operated at 120 mK. A TERABEAM 1550 (*TOPTICA Photonics AG*) photomixer continuous-wave (CW) source at room temperature emits a tunable signal in the range of 0.1–1 THz with a step size of 10 MHz and a bandpass filterstack inside the cryostat that defines a frequency band centered at $f = 346$ GHz. The source signal is attenuated with a beam splitter to keep the MKIDs in a linear operating regime. Frequency multiplexing readout electronics are used to enable simultaneous measurements of all FPRs [31]. Details on the setup can be found in [17], which is identical except for the cryogenic unit.

V. RESULTS AND DISCUSSION

A. Microwave resonators

We measure transmission dips of the μWRs at 50 mK as a function of readout power in the range of $P_{read} = -65$ to -157 dBm, as shown in Fig. 2(a) for μWR1. The internal quality factor Q_i of the resonator is then determined at each power from a Lorentzian fit [32]. We measure $S_{21}(f)$ from 4.7 to 6.7 GHz in 4001 points at $T = 60$ mK, excluding any points falling on a resonance feature, to create a 0-dB transmission reference. Figure 2(b) shows the resulting Q_i as a function of the average photon number in the resonator per $\lambda/2$, given by

$$\langle n_{ph} \rangle = \frac{P_{int}}{hf^2}, \tag{2}$$

where P_{int} is the internal power, given for the μWRs by $P_{int} = mQ^2 P_{read}/\pi Q_c$ with $m = 2$ or $m = 1$ for quarter-wave and half-wave resonators, respectively. All μWRs show a characteristic behavior for TLS loss and can be fitted using [33]

$$\frac{1}{Q_i} = \frac{\tanh(\hbar\omega/2k_b T)}{Q_{i,0}(1 + (\langle n_{ph} \rangle/n_s))^{\beta/2}} + \frac{1}{Q_r}, \tag{3}$$

where Q_i has a minimum value $Q_{i,0}$ at photon numbers below the saturation value n_s, increases with a slope given by β until other loss source dominate at high photon numbers, saturating at Q_r. As the CPW resonators do not contain a-Si, their TLS losses are dominated by
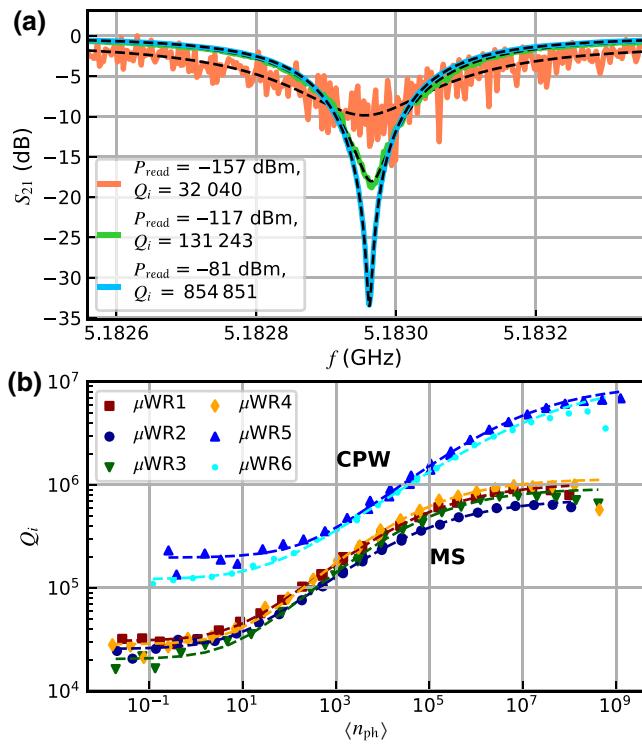
FIG. 2.   (a) Transmission for μWR1 at three different readout powers, with the respective Lorentzian fits shown by the black dotted lines. (b) Measured internal quality factor Q_i as function of $\langle n_{ph} \rangle$ for all μWRs shown as symbols, with fits of Eq. (3) shown by dotted lines with corresponding colors.

the metal-substrate and substrate-air interfaces, with crystalline Si as substrate [34]. Both $Q_{i,0}$ and Q_r values (μWR5: $Q_{i,0} \approx 2.0 \times 10^5$, $Q_r \approx 9.5 \times 10^6$. μWR6: $Q_{i,0} \approx 1.2 \times 10^5$, $Q_r \approx 9.9 \times 10^6$) are comparable with the state of the art for CPW resonators made of sputtered Nb-Ti-N [5], indicating an excellent film and interface quality for both the upper and lower Nb-Ti-N layers (sampled by μWR5 and μWR6, respectively) with no significant degradation due to the fabrication process. We find values of β between 0.7 and 0.8 for all resonators, which is consistent with the literature [33].

Losses in amorphous microstrips are generally dominated by TLS in the bulk dielectric layer [35]. We assume that losses in the metal-substrate interface can be neglected here, due to the surface layer quality shown by the CPW resonators. Consequently, the internal loss factor of the a-Si film, can be obtained as $Q_{i,\mathrm{aSi}}(6\ \mathrm{GHz}) = 27 \pm 4 \times 10^3$ from an average over all microstrip resonators and using

$$Q_{i,\mathrm{aSi}} = k_{\mathrm{fill}} \times Q_i \qquad (4)$$

with the filling factor $k_{\mathrm{fill}} = 0.96$ of the microstrip line, taking the a-Si layer overetch into account [see Fig. 1(e)]. This value corresponds to a loss tangent $\tan\delta = Q_i^{-1} = 3.7 \pm 0.5 \times 10^{-5}$, which is expected for

a-Si films [36]. We calculate the filling factor k_{fill} by simulating a short microstrip line in CST MICROWAVE STUDIO and varying the loss tangent of the dielectric. The relation between simulated line loss and the set loss tangent is then given by k_{fill}.

B. Fabry-Perot resonators

We measure the transmission through the four FPRs as a function of source frequency and apply a correction for directly coupled stray light, using the response of the blind MKID as introduced in Ref. [17]. Figure 3(b) shows the resulting spectra containing clear transmission peaks with an average frequency spacing dF corresponding to the different resonator lengths. Variations in peak height, as well as secondary peaks visible in FPR1, can be explained qualitatively by standing waves before the FPR modifying the transmission through the first coupler with a wavelength corresponding roughly to the electrical distance between antenna and FPR coupler. For each resonance peak, we obtain Q_L from a Lorentzian fit and the mode number from the resonance frequency F_n using $n = F_n/dF$. The standing waves before the FPR also introduce an oscillation in the measured Q_L, due to a modified Q_c.
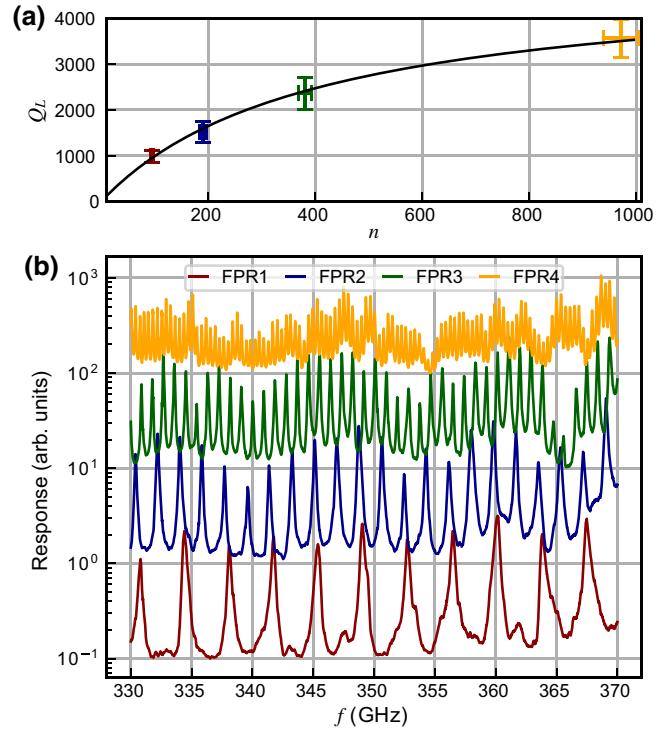

FIG. 3.   (a) Averaged loaded quality factor Q_L as a function of average mode number in the four FPRs. The fit using Eq. (1) is shown by the black line. (b) Measured spectra of the FPRs, offset along the y axis for better comparison. Line colors correspond to the markers in (a).

In this setup, we do not have an absolute reference for unity transmission and cannot, therefore, use the height of the FPR peaks to obtain Q_i and Q_c independently. However, as we are measuring different resonators, each designed with different mode numbers n at the same frequency, we can fit $Q_L(n)$ using Eq. (1) to retrieve $Q_{c,1}$ and Q_i. For this purpose, we take the mean value of Q_L for each resonator, as plotted in Fig. 3(a), while assuming that Q_L is linear with frequency and that the standing wave oscillations are sampled well enough to be averaged out. The resulting mean value then corresponds to the value at the center frequency of the measurement band, 350 GHz, whereas the error bars are a measure of both the statistical scatter and the linear slope over the averaged frequency range. A fit to Eq. (1) then results in $Q_{c,1} = 12.4 \pm 0.7$ and $Q_i = 4.9 \pm 0.3 \times 10^3$.

Following Eq. (4), we then obtain the internal loss factor of a-Si at 350 GHz as $Q_{i,\text{aSi}}(350 \text{ GHz}) = 4.7 \pm 0.3 \times 10^3$, corresponding to a loss tangent of $\tan \delta(350 \text{ GHz}) = 2.1 \pm 0.1 \times 10^{-4}$ which represents a significantly higher loss compared with the microwave regime, where $\tan \delta(6 \text{ GHz}) = 3.7 \pm 0.5 \times 10^{-5}$. Furthermore, we estimate the maximum incident power at the FPR to be less than 5 pW, placing the FPR in the single-photon regime with $n_{\text{ph}} < 8$. The increased loss at submillimeter wave frequencies is in disagreement with the TLS standard model, where a constant loss is predicted in the single-photon regime when $\hbar\omega \gg k_B T$, which is the case for both measurements.

A possible explanation of this discrepancy, could be a modified TLS model with a frequency dependent density of states $N(f)$. Such a model has been recently used to describe dephasing and noise due to TLS, combining interacting TLS with the power law of $N(f) \propto (f^\mu)$ with $\mu \approx 0.3$ obtained from noise measurements [37]. We find that a value of $\mu \approx 0.4$ would resolve the discrepancy in our measurement. Note, that the power dependence of $\beta < 1$ we find at microwave frequencies is also often identified with interacting TLS. Alternatively, it is possible that we observe the low-frequency tail of resonant phonon absorption peaks at far-infrared wavelengths. Room-temperature measurements of SiO_x and SiN in the far-infrared regime indicate that such a low-frequency tail could have the relevant magnitude [38,39]. Losses in the Nb-Ti-N film due to disorder effects should also be considered. However, we consider this highly unlikely to be the dominant effect, because measurements on a Nb-Ti-N CPW line with a similar film yield a $Q_i \approx 17 \times 10^3$ limited fully by radiation losses [17]. We also find no indication in DC or microwave measurements that the Nb-Ti-N film quality of either the top or bottom layer is degraded. The two CPW datasets in Fig. 2 represent a CPW line from each Nb-Ti-N layer. Further experiments in the 100–1000 GHz frequency range, in combination with microwave measurements, are needed to clarify this issue.

VI. CONCLUSION

In conclusion, we measured the losses of high-Q resonators made of Nb-Ti-N/a-Si/Nb-Ti-N microstrips in the single-photon regime at 6 and 350 GHz. In particular, we demonstrate an effective method to independently measure Q_i and Q_c at submillimeter wave frequencies without an absolute power calibration, using multiple FPRs on a single chip. This method can be easily extended up to the band-gap frequency of Nb-Ti-N around 1 THz. We measure a very low loss tangent for the a-Si film at microwave frequencies, with a power dependence that is consistent with TLS theory. At submillimeter wave frequencies, we find an unexpected increase in the loss tangent, which requires further investigation to identify the root cause.

APPENDIX: MODE NUMBER DEPENDENCE OF Q_C

In Goeppl *et al.* [40], an equation for the coupling Q-factor of a FPR ($Q_{\text{ext}} = Q_c$) is derived as

$$Q_{\text{ext}} = \frac{C}{2n\omega_0 R_L C_k^2} \tag{A1}$$

with the real load impedance $R_L = 50 \ \Omega$, the coupling capacitance C_k, and the resonator capacitance $C = C_l l/2$, where C_l is the capacitance per unit length and l is the resonator length. This equation apparently shows a mode number dependence $Q_{\text{ext}} \propto 1/n$, which is seemingly in conflict with the dependence $Q_c \propto n$ used in this paper, which is based on the equation

$$Q_c = \frac{n\pi}{|S_{21,c}|^2}, \tag{A2}$$

where $S_{21,c}$ is the transmission through a single coupler. In the following appendix, we show the derivation of Eq. (A2), the equivalence between Eq. (A1) and (A2), the underlying reason for the apparent conflict in mode number dependence and, finally, why $Q_c \propto n$ should be used when considering the properties of a FPR.

Equation (A2) is based on the definition of the quality factor

$$Q = \frac{\omega E_{\text{stored}}}{P_{\text{loss}}}, \tag{A3}$$

where E_{stored} is the total energy stored in the resonator, whereas P_{loss} is the power loss per full resonator cycle.

The power loss per cycle through a single coupler of the FPR is given by

$$P_{\text{loss}} = NfE_{\text{stored}}|S_{2'1'}|^2, \tag{A4}$$

where $S_{2'1'}$ is the transmission through the coupler and N is the number of times the coupler is encountered per resonator cycle. For a half-wave resonator, N is given by the

mode number as $N = 1/n$. Combining Eqs. (A3) and (A4) then results in

$$Q_{c1} = \frac{n2\pi}{|S_{2'1'}|^2}.\tag{A5}$$

The second coupler can then be included to obtain the total coupling Q-factor as

$$\frac{1}{Q_c} = \frac{1}{Q_{c1}} + \frac{1}{Q_{c2}} = \frac{n\pi}{|S_{2'1'}|^2},\tag{A6}$$

where the latter relation retrieves Eq. (A2) for identical coupling strength on both sides ($Q_{c1} = Q_{c2}$).

In order to show the equivalence of $Q_{\text{ext}} = Q_c$, we start by taking the *ABCD* matrix of an isolated coupler as given by Goeppl *et al.* [40]

$$\begin{pmatrix} A & B \\ C & D \end{pmatrix} = \begin{pmatrix} 1 & \frac{1}{i\omega_n C_k} \\ 0 & 1 \end{pmatrix}\tag{A7}$$

with $\omega_n = n\omega_0$ and retrieve $S_{21,c}$ from it as

$$S_{21,c} = \frac{2}{2 + 1/(i\omega_n C_k R_L)},\tag{A8}$$

where we use

$$S_{21} = \frac{2}{A + B/R_L + CR_L + D}\tag{A9}$$

under the assumption that the characteristic line impedances Z_0 on either side of the coupler are matched to the load impedance R_L.

The absolute square $|S_{21,c}|^2$ then follows as

$$|S_{21,c}|^2 = \frac{4\omega_n^2 C_k^2 R_L^2}{1 + 4\omega_n^2 C_k^2 R_L^2} \approx 4\omega_n^2 C_k^2 R_L^2,\tag{A10}$$

where the approximation follows from the condition of a small capacitance ($\omega_n C_k R_L \ll 1$) as used by Goeppl *et al.* [40]. Note here the proportionality $|S_{21,c}|^2 \propto \omega_n^2$.

Combining Eqs. (A1) and (A10) then results in

$$Q_{\text{ext}} = \frac{2\omega_n CR_L}{|S_{21,c}|^2},\tag{A11}$$

which is not quite identical to Eq. (A2), but already follows its proportionality of $Q_{\text{ext}} \propto n$ due to $\omega_n = n\omega_0$.

We then use $v_{\text{ph}} = 1/\sqrt{(L_l C_l)}$, the line impedance $Z_0 = \sqrt{(L_l/C_l)}$ and L_l the inductance per unit length to obtain the identity of

$$\frac{\omega_n C_l l}{2} = \frac{\omega_n l}{v_{\text{ph}} Z_0},\tag{A12}$$

which we can rewrite, using $\omega_n/v_{\text{ph}} = 2\pi/\lambda$, $l/\lambda = n/2$ (for a half-wave resonator) and the matched impedance

condition $Z_0 = R_L$, as

$$\frac{\omega_n C_l l}{2} = \frac{n\pi}{R_L}.\tag{A13}$$

Substituting Eqs. (A13) in (A11) we finally obtain the form of Eq. (A2)

$$Q_{\text{ext}} = \frac{n\pi}{|S_{21,c}|^2} = Q_c.\tag{A14}$$

Note here, that the matched impedance condition is only used to easily show the equivalence, but is not necessary for either equation to be used on its own. For Eq. (A1) it is explicitly included due to the presence of R_L, whereas Eq. (A2) includes it implicitly as $S_{21,c}$ is obtained from electromagnetic simulations and can therefore account for any impedance mismatch. In addition, any impedance mismatch does not factor into the mode number dependence.

In order to explain the apparently conflict in mode number dependence, we suggest, that while Eq. (A1) is based on a flawless derivation and provides accurate fits to measurements [40], it conflates mode number dependence with frequency dependence of the coupler and therefore does not provide an accurate physical interpretation of the mode number dependence.

The frequency dependence of the coupler can be understood from Eqs. (A10) and (A11): the couplers used in both of the papers considered here are fundamentally high-pass filters operated in the stop-band regime and their transmission is therefore proportional as $|S_{21,c}|^2 \propto \omega^2$. Note, that we omit the subscript n here, as this proportionality exists independent from the resonant behavior of the FPR and must therefore be considered separate from the mode number.

Goeppl *et al.* [40] argue that Eq. (A1) shows $Q_{\text{ext}} \propto 1/n$. However, its primary dependence should be understood as $Q_{\text{ext}} \propto 1/\omega_n$ which, when taking the coupler transmission into account, becomes $Q_{\text{ext}} \propto \omega_n/\omega^2 \propto n/\omega^2$ [see Eq. (A11)]. In contrast, Eq. (A2) shows a clear separation of coupler properties ($S_{21,c}$) and mode number.

The difference shown here is usually not significant for single resonators, as both equations will yield the same results for Q_c. However, it needs to be taken into consideration when one wants to understand and exploit the fundamental behavior of a transmission line FPR.

---

[1] R. Barends, J. Kelly, A. Megrant, D. Sank, E. Jeffrey, Y. Chen, Y. Yin, B. Chiaro, J. Mutus, C. Neill, P. O'Malley, P. Roushan, J. Wenner, T. C. White, A. N. Cleland, and J. M. Martinis, Coherent Josephson Qubit Suitable for Scalable Quantum Integrated Circuits, Phys. Rev. Lett. **111**, 080502 (2013).

[2] F. Arute *et al.*, Quantum supremacy using a programmable superconducting processor, Nature **574**, 505 (2019).

[3] P. K. Day, H. G. LeDuc, B. A. Mazin, A. Vayonakis, and J. Zmuidzinas, A broadband superconducting detector suitable for use in large arrays, Nature **425,** 817 (2003).

[4] R. M. J. Janssen, J. J. A. Baselmans, A. Endo, L. Ferrari, S. J. C. Yates, A. M. Baryshev, and T. M. Klapwijk, High optical efficiency and photon noise limited sensitivity of microwave kinetic inductance detectors using phase readout, Appl. Phys. Lett. **103,** 203503 (2013).

[5] R. Barends, N. Vercruyssen, A. Endo, P. J. de Visser, T. Zijlstra, T. M. Klapwijk, P. Diener, S. J. C. Yates, and J. J. A. Baselmans, Minimal resonator loss for circuit quantum electrodynamics, Appl. Phys. Lett. **97,** 023508 (2010).

[6] A. Megrant, C. Neill, R. Barends, B. Chiaro, Y. Chen, L. Feigl, J. Kelly, E. Lucero, M. Mariantoni, P. J. J. O'Malley, D. Sank, A. Vainsencher, J. Wenner, T. C. White, Y. Yin, J. Zhao, C. J. Palmstrøm, J. M. Martinis, and A. N. Cleland, Planar superconducting resonators with internal quality factors above one million, Appl. Phys. Lett. **100,** 113510 (2012).

[7] B. Ho Eom, P. K. Day, H. G. LeDuc, J. Zmuidzinas, and A wideband, low-noise superconducting amplifier with high dynamic range, Nat. Phys. **8,** 623 (2012).

[8] A. Wagner, L. Ranzani, G. Ribeill, and T. A. Ohki, Demonstration of a superconducting nanowire microwave switch, Appl. Phys. Lett. **115,** 172602 (2019).

[9] M. Colangelo, D. Zhu, D. F. Santavicca, B. A. Butters, J. C. Bienfang, and K. K. Berggren, Compact and Tunable Forward Coupler Based on High-Impedance Superconducting Nanowires, Phys. Rev. Appl. **15,** 024064 (2021).

[10] B. A. Mazin, D. Sank, S. McHugh, E. A. Lucero, A. Merrill, J. Gao, D. Pappas, D. Moore, and J. Zmuidzinas, Thin film dielectric microstrip kinetic inductance detectors, Appl. Phys. Lett. **96,** 102504 (2010).

[11] S. Beldi, F. Boussaha, J. Hu, A. Monfardini, A. Traini, F. Levy-Bertrand, C. Chaumont, M. Gonzales, J. Firminy, F. Reix, M. Rosticher, S. Mignot, M. Piat, and P. Bonifacio, High q-factor near infrared and visible al2o3-based parallel-plate capacitor kinetic inductance detectors, Opt. Express **27,** 13319 (2019).

[12] M. J. Myers, K. Arnold, P. Ade, G. Engargiola, W. Holzapfel, A. T. Lee, X. Meng, R. O'Brient, P. L. Richards, H. Spieler, and H. T. Tran, Antenna-coupled bolometer arrays for measurement of the cosmic microwave background polarization, J. Low. Temp. Phys. **151,** 464 (2008).

[13] P. A. R. Ade *et al.*, ANTENNA-COUPLED TES BOLOMETERS USED IN BICEP2, Keck Array, AND SPIDER, Astrophys. J. **812,** 176 (2015).

[14] A. Endo *et al.*, First light demonstration of the integrated superconducting spectrometer, Nat. Astronomy **3,** 989 (2019).

[15] E. Shirokoff, P. S. Barry, C. M. Bradford, G. Chattopadhyay, P. Day, S. Doyle, S. Hailey-Dunsheath, M. I. Hollister, A. Kovács, C. McKenney, H. G. Leduc, N. Llombart, D. P. Marrone, P. Mauskopf, R. O'Brient, S. Padin, T. Reck, L. J. Swenson, and J. Zmuidzinas, in *Millimeter, Submillimeter, and Far-Infrared Detectors and Instrumentation for Astronomy VI*, edited by W. S. Holland, International Society for Optics and Photonics (SPIE, 2012), Vol. 8452, p. 209.

[16] G. Cataldo, E. M. Barrentine, B. T. Bulcha, N. Ehsan, L. A. Hess, O. Noroozian, T. R. Stevenson, K. U-Yen, E. J. Wollack, and S. H. Moseley, Second-generation design of micro-spec: A medium-resolution, submillimeter-wavelength spectrometer-on-a-chip, J. Low Temp. Phys. **193,** 923 (2018).

[17] S. Hähnle, N. v. Marrewijk, A. Endo, K. Karatsu, D. J. Thoen, V. Murugesan, and J. J. A. Baselmans, Suppression of radiation loss in high kinetic inductance superconducting co-planar waveguides, Appl. Phys. Lett. **116,** 182601 (2020).

[18] M. Spirito, G. Gentile, and A. Akhnoukh, in *82nd ARFTG Microwave Measurement Conference* (2013), p. 1.

[19] W. A. Phillips, REVIEW ARTICLE: Two-level states in glasses, Rep. Prog. Phys. **50,** 1657 (1987).

[20] C. L. Chang *et al.*, Low loss superconducting microstrip development at argonne national lab, IEEE. Trans. Appl. Supercond. **25** (2015).

[21] J. Gao, A. Vayonakis, O. Noroozian, J. Zmuidzinas, P. K. Day, and H. G. Leduc, Measurement of loss in superconducting microstrip at millimeter-wave frequencies, AIP Conf. Proc. **1185,** 164 (2009).

[22] A. Endo, C. Sfiligoj, S. J. C. Yates, J. J. A. Baselmans, D. J. Thoen, S. M. H. Javadzadeh, P. P. Van Der Werf, A. M. Baryshev, and T. M. Klapwijk, On-chip filter bank spectroscopy at 600–700 GHz using NbTiN superconducting resonators, Appl. Phys. Lett. **103,** 1 (2013).

[23] J. W. Lamb, Miscellaneous data on materials for millimetre and submillimetre optics, Int. J. Infrared Millimeter Waves **17,** 1997 (1996).

[24] L. Ferrari, O. Yurduseven, N. Llombart, S. J. C. Yates, J. Bueno, V. Murugesan, D. J. Thoen, A. Endo, A. M. Baryshev, and J. J. A. Baselmans, Antenna coupled mkid performance verification at 850 ghz for large format astrophysics arrays, IEEE Trans. Terahertz Sci. Technol. **8,** 127 (2018).

[25] D. J. Thoen, B. G. C. Bos, E. A. F. Haalebos, T. M. Klapwijk, J. J. A. Baselmans, and A. Endo, Superconducting nbtin thin films with highly uniform properties over a ∅ 100 mm wafer, IEEE Trans. Appl. Supercond. **27,** 1 (2017).

[26] B. T. Buijtendorp, J. Bueno, D. J. Thoen, V. Murugesan, P. M. Sberna, J. J. A. Baselmans, S. Vollebregt, and A. Endo, Characterization of low-loss hydrogenated amorphous silicon films for superconducting resonators, arXiv:2012.07692 (2020).

[27] S. Hähnle, O. Yurduseven, S. van Berkel, N. Llombart, J. Bueno, S. J. C. Yates, V. Murugesan, D. J. Thoen, A. Neto, and J. J. A. Baselmans, An ultrawideband leaky lens antenna for broadband spectroscopic imaging applications, IEEE Trans. Antennas Propag. **68,** 5675 (2020).

[28] S. J. C. Yates, A. M. Baryshev, O. Yurduseven, J. Bueno, K. K. Davis, L. Ferrari, W. Jellema, N. Llombart, V. Murugesan, D. J. Thoen, and J. J. A. Baselmans, Surface wave control for large arrays of microwave kinetic inductance detectors, IEEE Trans. Terahertz Sci. Technol. **7,** 789 (2017).

[29] P. J. de Visser, J. J. A. Baselmans, J. Bueno, N. Llombart, and T. M. Klapwijk, Fluctuations in the electron system of a superconductor exposed to a photon flux, Nat. Commun. **5,** 3130 (2014).

[30] D. F. Filipovic, S. S. Gearhart, and G. M. Rebeiz, Double-slot antennas on extended hemispherical and elliptical

silicon dielectric lenses, IEEE Trans. Microw. Theory Tech. **41**, 1738 (1993).

[31] J. van Rantwijk, M. Grim, D. van Loon, S. Yates, A. Baryshev, and J. Baselmans, Multiplexed readout for 1000-pixel arrays of microwave kinetic inductance detectors, IEEE Trans. Microw. Theory Tech. **64**, 1876 (2016).

[32] M. S. Khalil, M. J. A. Stoutimore, F. C. Wellstood, and K. D. Osborn, An analysis method for asymmetric resonator transmission applied to superconducting devices, J. Appl. Phys. **111**, 054510 (2012).

[33] M. Molina-Ruiz, Y. J. Rosen, H. C. Jacks, M. R. Abernathy, T. H. Metcalf, X. Liu, J. L. Dubois, and F. Hellman, Origin of mechanical and dielectric losses from two-level systems in amorphous silicon, arXiv:2008.07489 [cond–mat.mtrl-sci] (2020).

[34] J. Wenner, R. Barends, R. C. Bialczak, Y. Chen, J. Kelly, E. Lucero, M. Mariantoni, A. Megrant, P. J. J. O'Malley, D. Sank, A. Vainsencher, H. Wang, T. C. White, Y. Yin, J. Zhao, A. N. Cleland, and J. M. Martinis, Surface loss simulations of superconducting coplanar waveguide resonators, Appl. Phys. Lett. **99**, 113513 (2011).

[35] W. K.-G. Daalman, Ph.D. thesis, Delft University of Technology (2014).

[36] A. D. O'Connell, M. Ansmann, R. C. Bialczak, M. Hofheinz, N. Katz, E. Lucero, C. McKenney, M. Neeley, H. Wang, E. M. Weig, A. N. Cleland, and J. M. Martinis, Microwave dielectric loss at single photon energies and millikelvin temperatures, Appl. Phys. Lett. **92**, 112903 (2008).

[37] L. Faoro and L. B. Ioffe, Interacting tunneling model for two-level systems in amorphous materials and its predictions for their dephasing and noise in superconducting microresonators, Phys. Rev. B **91**, 014201 (2015).

[38] G. Cataldo, E. J. Wollack, A. D. Brown, and K. H. Miller, Infrared dielectric properties of low-stress silicon oxide, Opt. Lett. **41**, 1364 (2016).

[39] G. Cataldo, J. A. Beall, H.-M. Cho, B. McAndrew, M. D. Niemack, and E. J. Wollack, Infrared dielectric properties of low-stress silicon nitride, Opt. Lett. **37**, 4200 (2012).

[40] M. Göppl, A. Fragner, M. Baur, R. Bianchetti, S. Filipp, J. M. Fink, P. J. Leek, G. Puebla, L. Steffen, and A. Wallraff, Coplanar waveguide resonators for circuit quantum electrodynamics, J. Appl. Phys. **104**, 113904 (2008).